Standard Article

A comparative study of gasoline skeletal mechanisms under partial fuel stratification conditions using large eddy simulations

Gaurav Guleria[1] , Dario Lopez-Pintor[2], John E Dec[2] and Dimitris Assanis[1,3]

Abstract

Partial fuel stratification (PFS) is a low temperature combustion strategy that can alleviate high heat release rates of traditional low temperature combustion strategies by introducing compositional stratification in the combustion chamber using a split fuel injection strategy. In this study, a three-dimensional computational fluid dynamics (CFD) model with large eddy simulations and reduced detailed chemistry was used to model partial fuel stratification at three different stratified conditions. The double direct injection strategy injects 80% of the total fuel mass at -300 CAD aTDC and the remaining 20% of the fuel mass is injected at three different timings of -160, -50, -35 CAD to create low, medium, and high levels of compositional stratification, respectively. The PFS simulations were validated using experiments performed at Sandia National Laboratories on a single-cylinder research engine that operates on RD5-87, a research-grade E10 gasoline. The objective of this study is to compare the performance of three different reduced chemical kinetic mechanisms, namely SKM1, SKM2, and SKM3, at the three compositional stratification levels and identify the most suitable mechanism to reproduce the experimental data. Zero-dimensional chemical kinetic simulations were also performed to further understand differences in performance of the three reduced chemical kinetic mechanisms to explain variations in CFD derived heat release profiles. The modeling results indicate that SKM3 is the most suitable mechanism for partial fuel stratification modeling of research-grade gasoline. The results also show that the autoignition event progresses from the richer to the leaner compositional regions in the combustion chamber. Notably, the leaner regions that have less mass per unit volume, can contribute disproportionately more toward heat release as there are more cells at leaner equivalence ratio ranges. Overall, this study illuminates the underlying compositional stratification phenomena that control the heat release process in PFS combustion.

Keywords

Low-temperature combustion, large-eddy simulations, partial fuel stratification, computational fluid dynamics, homogeneous charge compression ignition, gasoline surrogate, reduced chemical kinetic mechanism, skeletal kinetic mechanism

Introduction

Engine researchers have been conducting research efforts on low temperature combustion (LTC) engines since the late '70s. The potential to achieve higher engine thermal efficiencies while maintaining ultra-low NO_x and soot emissions can satisfy both the demand to increase fuel efficiency of internal combustion engines while also meeting increasingly stricter emissions regulations.

Homogeneous Charge Compression Ignition (HCCI) is one of the low temperature combustion concepts that can overcome the shortcomings of conventional SI and CI engines with respect to throttling losses and engine-out emissions, respectively.[1–3] HCCI uses a homogeneous mixture achieved by either

[1]Department of Mechanical Engineering, Stony Brook University, Stony Brook, NY, USA
[2]Sandia National Laboratories, Livermore, CA, USA
[3]Institute for Advanced Computational Science, Stony Brook University, Stony Brook, NY, USA

Corresponding author:
Dimitris Assanis, Department of Mechanical Engineering, Stony Brook University, 100 Nicolls Road, Stony Brook, NY 11794, USA.
Email: dimitris.assanis@stonybrook.edu

port fuel injection or early direct injection (DI),[4] leading to a flameless sequential autoignition process as has been shown by optical diagnostics studies.[5–7]

While HCCI can reduce both NO_x and soot emissions and simultaneously achieve high thermal efficiency, its operating range still remains limited due to lack of control of the heat release process. The autoignition timing and rate are dominated by chemical kinetics and state conditions the charge mixture experiences during the compression stroke. Engines operating on the HCCI combustion regime can easily suffer from misfires and low combustion efficiency at low loads and excessive heat release and pressure rise rates at high loads.

A number of different combustion strategies have been proposed to increase the control and consequently the operating range of HCCI combustion, thus potentially making it more commercially viable. Initial studies showed that using Negative Valve Overlap (NVO) to dilute the mixture along with Exhaust Gas Recirculation (EGR) assisted in controlling the heat release rate.[8–13] Subsequently, variable compression ratio,[14–17] spark-ignition assistance,[18–21] and intake boosting[22–27] have also been investigated to alleviate the excessive heat release rates and thus can increase the load range of HCCI.

Researchers have also investigated the effects of thermal stratification on HCCI combustion to extend the load limit of HCCI engines.[28] Thermal stratification in the combustion chamber results in cascading auto ignition events, where the hottest zones in the cylinder ignite first and subsequently colder zones follow, which leads to staggered heat release. It should be noted that, in a real engine, naturally occurring thermal stratification develops due to wall heat transfer and turbulent convection. Therefore, despite the fact that this phenomenon has been used in multiple numerical and experimental studies to smoothen the high heat release rate, it is intrinsic to the engine and hard to control.

In theory, it should be possible to significantly extend the load limit by increasing the thermal stratification. For instance, Sjöberg et al.[29] showed that increasing the thermal stratification leads to reduced pressure rise rates and increasing the thermal width by 10 K at bottom dead center (BDC) piston position can successfully stagger the combustion enough so that the equivalence ratio limit can be extended from 0.44 to 0.60. Some experimental techniques were proposed to practically control the in-cylinder thermal stratification in a real engine. For example, Sjöberg and Dec[30] have investigated direct injection of ethanol around −80 crank angle degrees (CAD) after top dead center (aTDC) to introduce thermal stratification in the cylinder. The study used 60%–70% of premixed charge and 30%–40% of the fuel as direct injection. The results showed high rates of evaporative cooling compared to gasoline and lower heat release rate compared to homogeneous fuel/air mixture, thereby staggering the

auto ignition. However, controlling thermal stratification using practical methods and without increasing heat losses has proven difficult.

Many researchers have studied other LTC approaches that introduce compositional stratification in the combustion chamber to control the heat release rate in HCCI by sequential auto ignition as thermal stratification is very difficult to control. Compositional stratification is attained by direct fuel injection which helps in controlling combustion. Dempsey et al.[31] have classified different LTC modes on the basis of stratification achieved in the combustion chamber. Some of the popular LTC strategies are Premixed Charge Compression Ignition (PCCI),[32–37] Reactivity Controlled Compression Ignition (RCCI),[38–41] Gasoline Direct Injection Compression Ignition (or GDCI),[42,43] Gasoline Compression Ignition (GCI)[44,45] and Partial Fuel Stratification (PFS).

In PCCI, high reactivity fuel (e.g. diesel) is injected early during the compression stroke and the combustion phasing is controlled by changing the injection parameters. Kook and Bae[37] have showed that PCCI shows reduction in nitrogen oxides (NO_x) by 90%, however hydrocarbons (HC) and carbon monoxide (CO) emissions increased compared to conventional diesel engines. RCCI is another LTC strategy that uses two different fuels to control the combustion. In RCCI, the low reactivity fuel is port fuel injected to form a homogeneous mixture and the high reactivity fuel is directly injected during the compression stroke. Researchers have been able to achieve higher load range and lower emissions using RCCI however, the requirement of two different fuel systems is a potential barrier to large-scale commercialization of RCCI due to increased complexity of the system. The GCI strategy involves direct injection of gasoline near TDC to increase in homogeneity in the fuel/air mixture thus controlling the heat release. However, GCI also leads to higher particulate matter emissions and requires the use of a particulate filter to keep the emissions within regulations.

Partial Fuel Stratification was proposed by Sjöberg and Dec[46] as another LTC strategy to control the heat release rate. PFS utilizes a split injection strategy to create compositional stratification in the combustion chamber.[47–50] Sjöberg and Dec[46] showed that PFS can be used to increase the load range by using fuels that are sensitive to the local equivalence ratio and this behavior was named as ϕ-sensitivity of the fuel. Dec et al.[47] also investigated PFS using gasoline at boosted conditions. Gasoline is not very ϕ-sensitive at naturally aspirated conditions, but it shows moderate ϕ-sensitivity at an intake pressure of 1.6 bar and high ϕ-sensitivity at an intake pressure of 2.0 bar. Their study showed that gasoline can be used for PFS under boosted conditions and it can decrease the peak of heat release rate. An increase in load range of the engine and very low NO_x and soot emissions were also observed. PFS also showed higher thermal efficiency as advanced

combustion phasing was achieved without triggering knock. Yang et al.[48] studied the effects of engine speed, intake temperature, and fuel composition on PFS using PRF73 and Hydrobate (a 73-RON gasoline). In their study, they showed that ϕ-sensitivity does not change as the engine speed is increased. The increase in intake temperature from 333 to 447 K reduces the ϕ-sensitivity of PRF73 fuel. The effect of fuel composition was studied by comparing PRF73 to Hydrobate which have comparable HCCI reactivities. The study showed that both the fuels had similar decrease in pressure rise rate at 1200 and 1600 rpm, which implies that overall HCCI reactivity of the fuel is the more important parameter than specific components in the fuel.

A significant number of numerical studies done on HCCI engines show the importance of using suitable reduced chemical kinetic mechanisms to accurately predict the combustion. It has been shown that accurate results using multi-zone modeling methodology can be obtained for long chain hydrocarbons using reduced chemical kinetic mechanisms.[51,52] Fiveland and Assanis[53] developed a model for HCCI engines under turbocharged conditions. Their study coupled chemical kinetics with sub models for physical processes in the HCCI engine. The model predicted peak pressure and burn duration within the standard deviation values. However, predictions for the CO emissions were under predicted. The authors recommended more complex computational fluid dynamics (CFD) modeling scheme coupled with a more robust chemical kinetic mechanism to accurately predict emissions. Kong and Reitz[54] modeled combustion in a HCCI engine by coupling CHEMKIN with KIVA. Their model predicted ignition delay accurately for a range of operating conditions. Jia and Xie[55] compared different chemical kinetic mechanisms for iso-octane and showed that the ignition delay is significantly affected by local pressure, temperature, and equivalence ratio. The authors also proposed a new skeletal iso-octane mechanism that was validated for HCCI applications.

In spite of all the encouraging experimental studies, there have been very few studies that investigate the fundamental processes that control ignition in PFS. Particularly, previous work performed by Priyadarshini et al.[56] numerically investigated low levels of charge-mixture stratification from an early second injection. This study extends upon this previous work by using a 3D CFD model with detailed chemistry employing Large Eddy Simulations (LES) to study PFS under low, moderate, and highly stratified operating conditions. The study uses research grade gasoline coupled with moderate boosting to investigate the performance of three different skeletal chemical kinetic mechanisms, namely SKM1, SKM2, and SKM3 and their respective surrogate fuels. The objective of this study is to investigate the performance, limitations, and suitability, of the three chemical kinetic mechanisms considered for PFS modeling at different levels of ϕ stratification. An appropriate mechanism, SKM3, is ultimately identified

and employed in the 3D CFD model to study the effects of the second injection timing on fuel distribution and its subsequent impact on the start and progression of ignition.

# Experimental setup and model development

Experiments

The current study is based on the experimental data gathered at Sandia National Laboratories (SNL). The engine used to collect the experimental data[57] is a Cummins B-series six (6) cylinder medium-duty engine in which five cylinders have been deactivated to effectively create a single-cylinder combustion engine. The fuel used in the experiments is a research-grade regular E10 gasoline named RD5-87 that has been used for recent research in industry, academia, and at national laboratories.[58,59] The intake pressure was 1.3 bar, and the engine speed was 1200 rpm. The engine had eight (8) CAD of positive valve overlap, which minimized the residual gas trapping. The experiments also used an 80−20 split injection strategy where two fuel injections were performed every engine cycle. The first injection starts at −300 CAD aTDC during the intake stroke and 80% of the fuel mass was injected. The rest of the 20% fuel mass is injected during the second injection (SOI$_2$) event. The timing of second injection is retarded from −160 to −35 CAD aTDC to vary the level of fuel stratification in the chamber. The injection pressure was 120 bar, and the intake temperature was kept constant at 397 K for the study. All the engine specifications and the operating conditions are summarized in Table 1. Further details about the experimental data used in this investigation can be found in Gentz et al.[60] and Lopez-Pintor.[61]
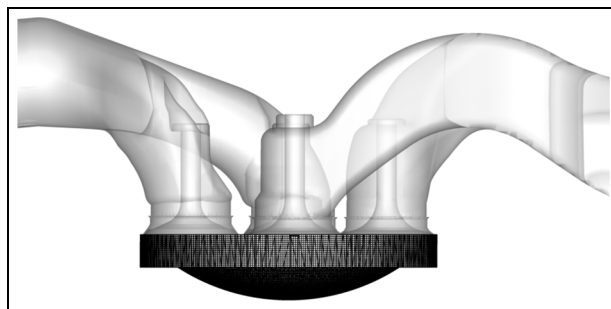
CFD model

The 3D CFD model used in the current study is shown in Figure 1. The model is built using Converge CFD v 2.4[62] and consists of three regions: the intake ports, the exhaust ports, and the combustion chamber. Each region was initialized separately based on experimental data. An orthogonal cut cell grid[63] with fixed embedding was used in the model to create a mesh of 0.7 mm in the combustion chamber and around the valves, and 0.175 mm around the fuel injector as shown in Figure 2. The engine has been used in the previous CFD study as well.[56] The cylinder wall temperature was estimated by extrapolating the fire deck temperatures.[64] The liquid properties database available in Converge v2.4 was used to describe the physical properties of gasoline surrogates used in the study. The turbulence is resolved by using a LES framework to better capture unsteady flow behavior. In the current study, the Dynamic Structure turbulence model[65] using Favre filtering was used.

Table 1. Engine specifications and operating conditions.

Engine	Cummins medium-duty engine
Displaced volume	0.98 L
Stroke	120 mm
Bore	102 mm
Connecting rod	192 mm
Compression ratio	14:1
Intake valve opening	−360 CAD aTDC
Intake valve closing	−158 CAD aTDC
Exhaust valve opening	122 CAD aTDC
Exhaust valve closing	−352 CAD aTDC
Valve overlap	+8 CAD
Engine speed	1200 rpm
Fuel delivery method	Direct injection
Intake pressure	1.3 bar
SOI_1 timing	−300 CAD aTDC
SOI_2 timing	−160 to −35 CAD aTDC
Equivalence ratio (ϕ)	0.37
Intake air temperature	397 K
Injector	Bosch HDEV 5.1
Injection pressure	120 bar
Total fuel mass	28.30 ± 0.04 mg/cycle
Fuel mass fraction in first injection	80%
Fuel mass fraction in second injection	20%
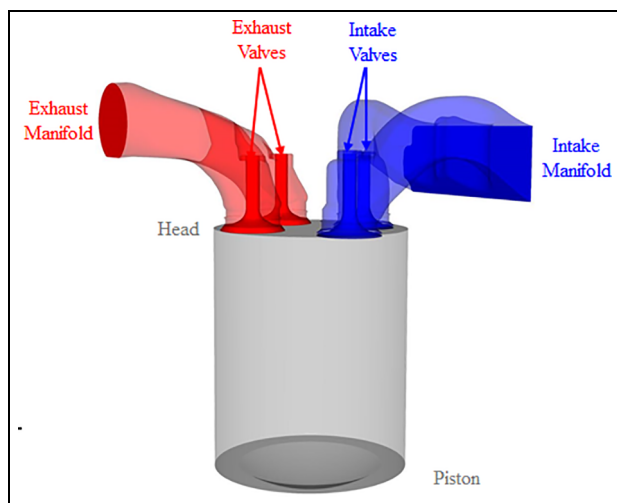
Figure 1. CFD model of the medium-duty Cummins B-series engine showing regions; combustion chamber (gray), intake ports (blue), and exhaust ports (red).

Spray sub models were used to capture several phenomena from the start of fuel injection to fuel vaporization. The spray breakup was captured using the Kelvin–Helmholtz and Rayleigh–Taylor (KH-RT) hybrid model[66,67] which takes into account the Kelvin-Helmholtz (KH) and the Rayleigh-Taylor (RT) instability models. The droplet evaporation is modeled using the Frossling evaporation model.[68] No Time Counter (NTC) Collision model is used to model the droplet collision as the computational cost of NTC collision model[69] increases linearly as the number of parcels increases, thereby allowing the use of higher

Figure 2. Computational domain of the 3D CFD model of the medium-duty Cummins B-series engine at −20 CAD aTDC.

number of parcels. The droplet drag coefficient was modeled using the Taylor Analogy Break-Up (TAB) model.[70] For simulating the interaction between the spray droplets and the walls, O'Rourke and Amsden[71] wall film model was used.

The combustion was modeled using the SAGE detailed chemical kinetic solver[72] coupled with multi-zone model by Babajimopoulos et al.[73] The wall heat transfer was modeled using the law of the wall model by Amsden and Findley[74] and the wall shear stress was calculated using Werner and Wengle law of the wall model.[75]

Chemical kinetic mechanisms

Three different skeletal chemical kinetic mechanisms, termed SKM1, SKM2, and SKM3 were used in this work.[56,76] These mechanisms were generated by reducing a 2878-species detailed mechanism for gasoline surrogates recently developed by Lawrence Livermore National Laboratory (LLNL).[77] The reduction was performed based on a large set of extinction residence times and ignition delays of a 7-species surrogate fuel for RD5-87 proposed by Lopez-Pintor et al.,[78] termed SV0 in this study and the composition of which is shown in Table 2. Extinction residence times were obtained in a perfectly stirred reactor (PSR) for a pressure variation from 1 to 50 bar, an equivalence ratio variation from 0.3 to 1.5, and an inlet temperature equal to 300 K. Ignition delays were obtained in a closed, homogeneous, constant-volume reactor for a pressure variation from 1 to 50 bar, an equivalence ratio variation from 0.3 to 1.5, and a temperature variation from 600 to 1600 K. Directed Relation Graph (DRG) was first applied to reduce the detailed mechanism with high efficiency, leading to an intermediate mechanism that was further reduced by applying DRG Aided Sensitivity Analysis (DRGASA). It should be noted that the LLNL detailed mechanism used in this investigation includes the chemistry of more than 50 single-component fuels, and most of them are not involved in the formulation of the surrogate fuels. For instance, the LLNL detailed mechanism includes sub-mechanisms for heavy aromatics (such as 1, 3, 5

Table 2. Formulation of the surrogates in % mole.

Surrogate	N-pentane (%)	Iso-octane (%)	1-Hexene (%)	Cyclo-pentane (%)	Toluene (%)	Ethanol (%)	N-heptane (%)	To use with
SV0	9	29	6	7	20	20	9	SKM2 and SKM3
SV1	16.5	23.8	5.90	12.4	21.3	20.1	0	SKM1

trimethylbenzene or p-xylene), branched olefins (such as di-isobutylene), alcohols (such as tert-butanol or n-pentanol) or furans (such as 2-methyl furan), the chemistry of which is not relevant for the surrogates and that it is easily eliminated by the DRG method. Only the chemistry of the hydrocarbons involved in the formulation of the surrogates was included in the reduced mechanisms, allowing for a more effective reduction. An in-house routine was applied to ensure the consistency of the mechanisms. This procedure resulted in SKM1 and SKM2 which have 152 species and 563 reactions as well as SKM3 which has 164 species and 582 reactions.

Optimization was applied to the skeletal mechanism to improve the prediction of ignition delays, and different optimization strategies led to the different skeletal mechanisms used in this study (SKM1, SKM2, and SKM3). SKM1 resulted from optimization using a simpler surrogate fuel, termed SV1 and the composition of which is shown in Table 2. Note that the 7-species SV0 surrogate has n-heptane whereas the 6-species SV1 surrogate does not. Thus, the combination of SKM1 and SV1 makes the description of the chemistry simpler, allowing a lower computational cost. SKM2 resulted from optimization using SV0. Finally, SKM3 resulted from optimization using SV0 and assigning a higher weighting factor to the ignition delay data of equivalence ratios higher than $\phi = 0.7$ (range of ϕ s that have shown to be important under stratified conditions, as it will be discussed in the following section).

Results and discussion

Compositional stratification analysis

The CFD model was used to reproduce experimental data from Sandia from Gentz et al.[60] The experiments were taken using a split injection strategy where the first injection (SOI$_1$) was fixed at -300 CAD aTDC and the second injection (SOI$_2$) was varied from -160 to -35 CAD aTDC. During SOI$_1$, 80% of the fuel mass was injected and the remaining 20% was injected at SOI$_2$. Gentz et al.[60] showed in their experiments that the combustion could be phased earlier without an extreme increase in pressure rise rate and NO$_x$ emissions by delaying SOI$_2$ as it increases the compositional stratification in the cylinder and staggers the combustion. For instance, the crank angle corresponding to 50% of the fuel mass burned by combustion, CA50, advances from 14.0 to 6.5 CAD aTDC as the SOI$_2$ retards from -160 to -35 CAD aTDC. The CFD simulations were performed for three operating conditions of SOI$_2$ equal to -160, -45, and -35 CAD aTDC using SKM1, SKM2, and SKM3. For this study, the simulations were run for seven (7) consecutive cycles. The comparison with the experiments was done using five (5) cycles as the first two (2) cycles were discarded to eliminate the influence of initial conditions. The CFD model was run on Seawulf high performance computing cluster that has 164 compute nodes, each with two Intel Xeon E5-2683v3 CPUs and each node has 28 cores. The model used 112 cores to run and each individual run took approximately 14 days to complete.

The intake temperature was adjusted in the simulations to replicate the experimental CA50. The increase in intake temperature for each case is shown in Table 3. This methodology allows to compensate for uncertainties in the heat transfer during the intake stroke, in some boundary conditions (such as the wall temperatures), and in the accuracy of the chemical models. The intake valve closing (IVC) temperature deviation between the experiments and the simulations was considered a metric for the accuracy of the simulations. Note that the IVC temperature is more representative of the compressed-gas temperature than the intake temperature, especially considering the uncertainties during the intake stroke. Note also that the CFD model was previously validated against experiments under motoring conditions, and the effective compression ratio of the CFD model was adjusted to account for uncertainties in heat losses of the closed cycle, blow by losses and deformations.[56] Therefore, the IVC temperature deviation should not be affected by these uncertainties. Despite the fact that the spray and mixing models were also validated against experimental data,[56] the uncertainty in the fuel distribution might be somehow masked by the IVC temperature deviation. Nevertheless, considering the limitations of both CFD models and experimental methods, simulations with low IVC temperature deviation will be considered accurate independently of the intake temperature deviation, since matching the experimental IVC temperature indicates that the simulations properly replicate the compressed-gas reactivity of the experiments. Values of the IVC temperature deviation will be reported and discussed in the following section.

The operating conditions were chosen to provide significant range of equivalence ratio stratification in the

Table 3. Increase in intake temperature (K).

SOI$_2$ (aTDC)	SKM 1	SKM 2	SKM 3
−160	9	13	17
−50	6	9	17
−35	1	1	18
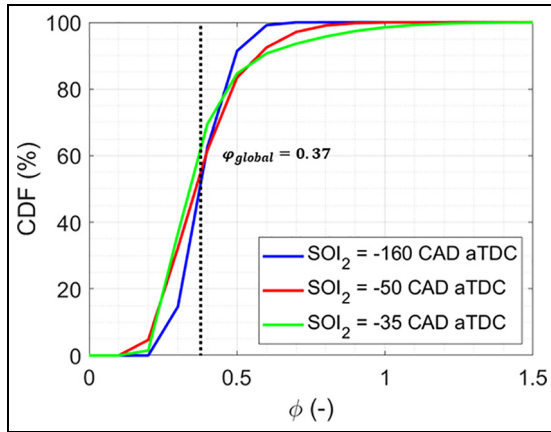
Figure 3. Ensemble averaged CDF of mass as a function of the local equivalence ratio (ϕ) in the combustion chamber at TDC, for SOI$_2$ = −160 CAD aTDC (blue), SOI$_2$ = −50 CAD aTDC (red), and SOI$_2$ = −35 CAD aTDC (green).

combustion chamber. Figure 3 shows the Cumulative Distribution Function (CDF) of mass in the combustion chamber plotted with equivalence ratio for the second injection timings of −160, −50, and −35 CAD aTDC at TDC. The dotted black line shows the global equivalence ratio of the mixture mass which is 0.37. The plot shows the range of equivalence ratio stratification that can be achieved in PFS combustion by changing the timing of second injection. For SOI$_2$ = −160 CAD aTDC, the local equivalence ratio ranges from 0.2 to 0.6 which shows low stratification in the combustion chamber. When the second injection is retarded to −50 CAD aTDC, it can be seen that the mixture stratification has increased as the fuel gets significantly less time to mix. This leads to equivalence ratio stratification between 0.18 and 0.80, which shows the mixture is moderately stratified. On retarding the second injection timing even further to −35 CAD aTDC, it is observed that the mixture stratification increases even further as the fuel is getting even less time to mix which leads to a higher equivalence ratio stratification range between 0.15 and 1.02 and shows that the mixture is highly stratified. It can also be observed that for second injection timings of −160 and −50 CAD aTDC, almost 56% of the mixture mass is below the global equivalence ratio of 0.37. For SOI$_2$ of −35 CAD aTDC, almost 65% of the mixture mass is below the global equivalence ratio of 0.37. The SOI$_2$ = −160, −50, and −35 CAD cases will be referred hereafter as low, moderately, and highly stratified cases, respectively.

Finally, it should be noted that the CFD model used in this investigation has been already validated by Priyadarshini et al.[56] for low and moderate levels of stratification and using SKM1. The current paper extends the work of Priyadarshini et al.[56] by evaluating two additional mechanisms and by extending the test matrix to include highly stratified conditions. Details on the validation of the CFD model can be found in Priyadarshini et al.[56]

Evaluation of SKM1, SKM2, and SKM3

A comparison of different combustion metrics between the experiments and the model is shown in Figure 4. Results are shown for low (top), moderate (middle), and high (bottom) levels of stratification. The CA10, CA50, CA90, CA10–50 duration, CA10–90 duration, peak pressure, peak heat release, and IVC temperature are plotted for the experiments (red) and for simulations (blue) with SKM1, SKM2, and SKM3. The experimental values are the average of 100 consecutive cycles and the error bars represent the standard deviation of the experiments where the total height of the error bars is two sigma. The numerical values are the ensemble average of five (5) consecutive runs of the CFD model.

The top row of Figure 4 shows the results for low stratification (SOI$_2$ = −160 CAD aTDC). It can be observed that for all the combustion metrics, the model is in very good agreement with the experiments when SKM1 is used. However, when SKM2 is used for this operating condition a large deviation for CA10 and CA50 is observed. The deviation is by a similar value of CAD and that why the CA10–50 duration is still close to the experiments. There are deviations observed for CA90, CA10–90, and peak heat release for SKM2 which shows that SKM2 is not able to predict the combustion for this operating condition. SKM3 is in close agreement with the experiments. The IVC temperature is within the experimental uncertainty for SKM1 and SKM3, which suggests that the intake temperature adjustment imposed in the simulations properly compensates for uncertainties during the intake stroke and the model accurately predicts the reactivity of the experiments. However, SKM2 shows the largest IVC temperature deviation which suggests a poor performance of the mechanism.

The middle row of Figure 4 shows the results for moderate stratification (SOI$_2$ = −50 CAD aTDC). It can be seen that SKM1 is in acceptable agreement with the experiments. Earlier CA10 and delayed CA90 explain the deviation of CA10–90 for the simulations from the experiments. Peak heat release is predicted lower than the experiments. SKM2 predicts an earlier CA10, later CA50, and a very late CA90. The prediction for peak pressure is good and the peak heat release is very low in simulations. It can be observed that simulations using SKM3 have very good agreement with the experiments at this operating condition. The predictions for CA10, CA50, and CA90 and peak pressure
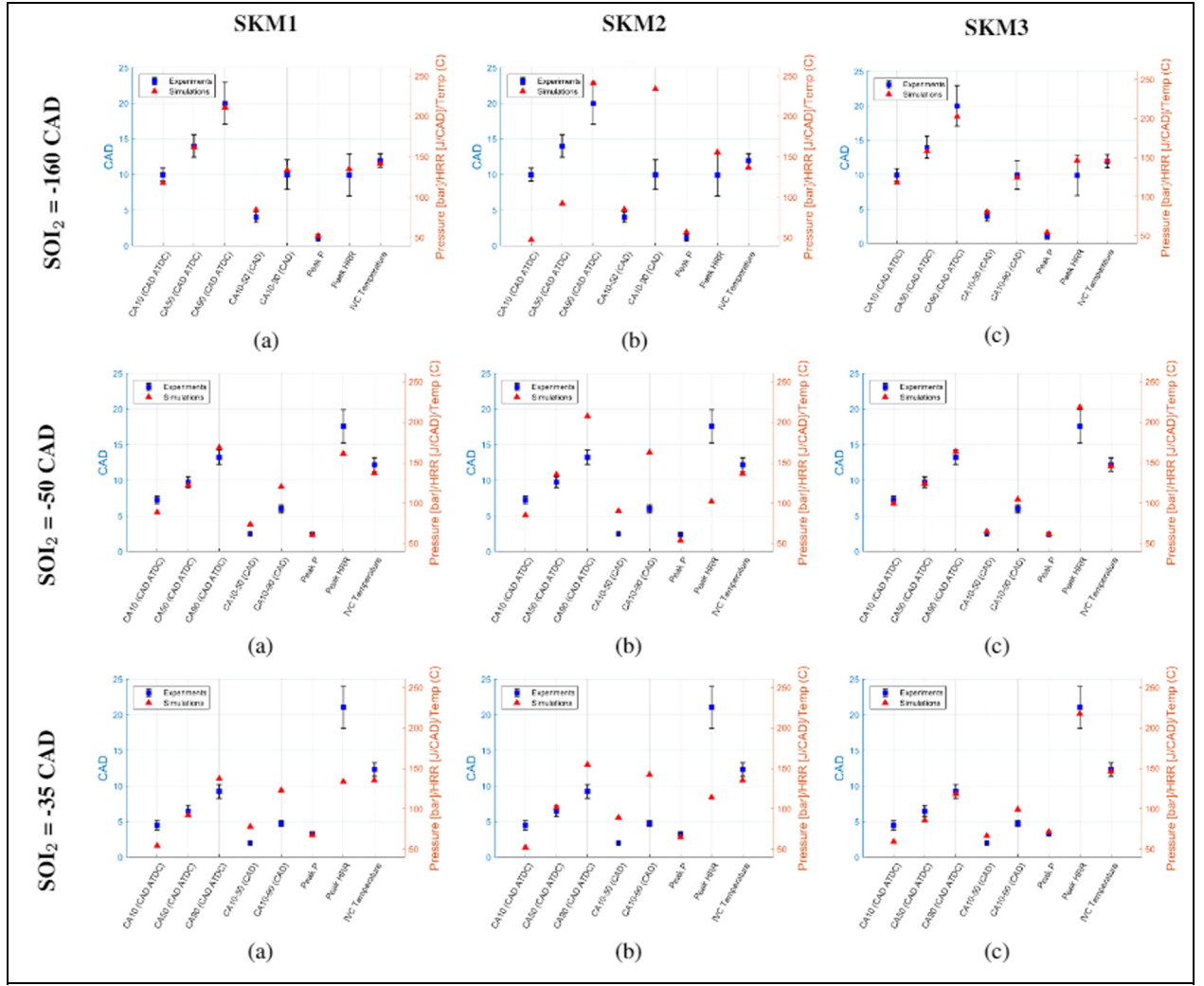
Figure 4. Combustion metrics for experiments (blue) and simulations (red). Top: low stratified conditions (SOI$_2$ = −160 CAD aTDC). Middle: moderately stratified conditions (SOI$_2$ = −50 CAD aTDC). Bottom: highly stratified conditions (SOI$_2$ = −35 CAD aTDC). Simulations were performed with SKM1 (a), SKM2 (b), and SKM3 (c).

are very close to the experiments. SKM3 can predict the auto ignition and progression of combustion very well for second injection timing of −50 CAD aTDC. Only SKM3 shows an IVC temperature within the experimental uncertainty, which suggests that SKM3 replicates the chemical kinetics of the fuel better than the other two mechanisms.

The bottom row of Figure 4 shows the results for high stratification (SOI$_2$ = −35 CAD aTDC). It can be seen that SKM1 predicts the CA10 early in the simulations and that is followed by delayed CA90, which shows earlier ignition and slower combustion than the experiments. This leads to deviation in the values of CA10–50 and CA10–90 for the simulations compared to the experiments. Peak heat release is also much lower in the simulations. SKM1 does not accurately predict auto ignition and progression of combustion at this highly stratified operating condition. A very similar trend is seen when simulations are run using SKM2. CA10 prediction is very close to values seen in SKM1. CA90 is more delayed compared to SKM1 and peak

heat release is even lower. SKM2 is not predicting combustion accurately as well for SOI$_2$ of −35 CAD aTDC. SKM3 still predicts earlier CA10 but compared to SKM1 and SKM2 it is closer to the experiments. SKM3 is also predicting CA50, CA90, peak pressure, and peak heat release more accurately than SKM1 and SKM2. As also happens for moderate levels of stratification, only SKM3 shows an IVC temperature within the experimental uncertainty, which further demonstrates the good performance of SKM3 compared to the other two mechanisms.

Figures 5 to 7 show the in-cylinder pressure and heat release rates (HRR) for simulations with SKM1, SKM2, and SKM3, respectively. Results for the three levels of stratification (low, moderate, and high) are plotted. For intelligibility, the first twenty (20) consecutive experimental cycles (gray) are plotted out of the set of hundred (100) cycles along with the five (5) consecutive LES cycles (colored) in the figures.

Figure 5(a) shows that the model is showing very good agreement with the experimental pressure and
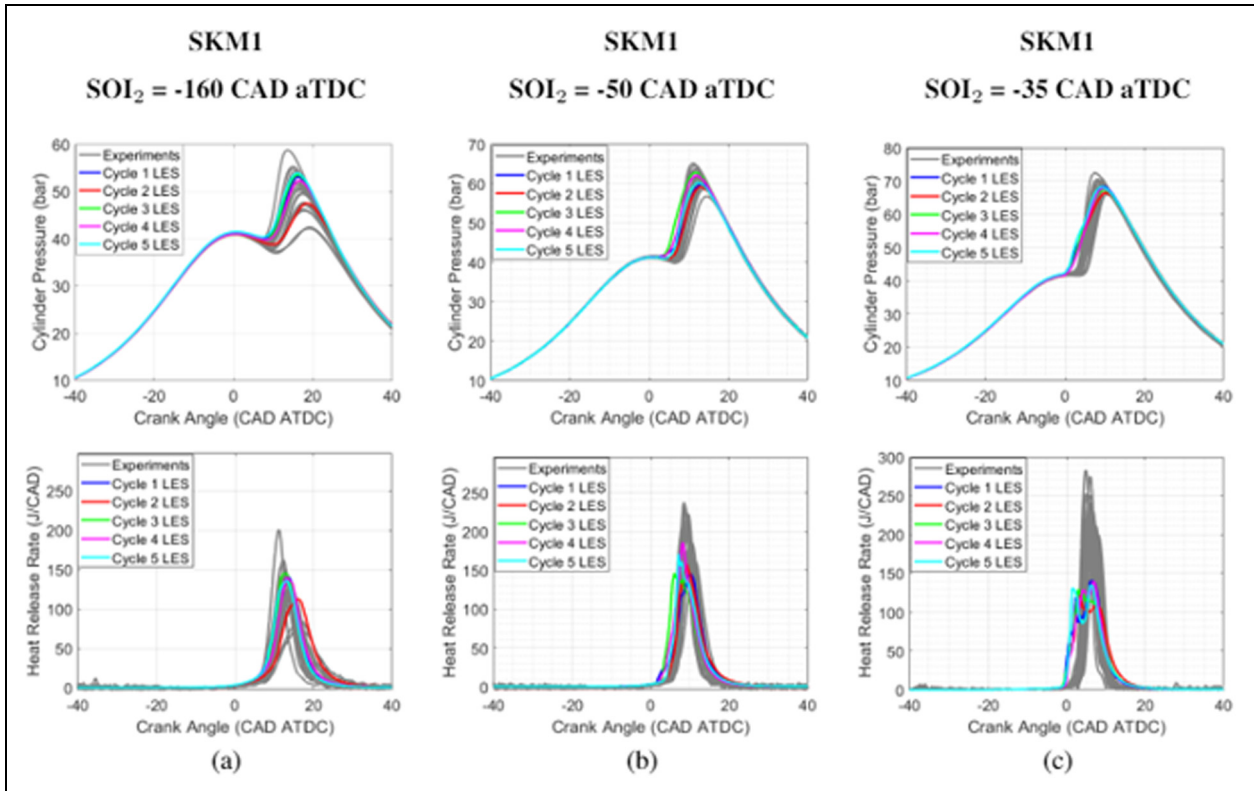
Figure 5. CFD results with SKM1. In-cylinder pressure (top) and HRR (bottom) are plotted for 20 consecutive experimental cycles (gray) and five consecutive LES cycles (colored) at $SOI_2 = -160$ CAD aTDC (a), $SOI_2 = -50$ CAD aTDC (b), and $SOI_2 = -35$ CAD aTDC (c).

heat release data for $SOI_2 = -160$ CAD aTDC using SKM1. The model is also able to capture cycle to cycle variation that shows good agreement with the experiments. For $SOI_2 = -50$ CAD aTDC, it can be observed that start of ignition in the model is a little advanced compared to the experiments as shown in Figure 5(b). The peak pressure and heat release are also lower compared to the experiments. For this operating condition SKM1 has acceptable agreement. For $SOI_2 = -35$ CAD aTDC, the model is igniting earlier than the experiments as seen in Figure 5(c). The pressure and peak heat release are lower and two peaks can be observed in the heat release profile for this operating condition. From the results it can be concluded that SKM1 is able to capture the experiments well for low and moderately stratified conditions, while for highly stratified conditions SKM1 does not show agreeable results.

A similar comparison was performed for the same operating conditions using SKM2. Figure 6(a) shows the performance of SKM2 at second injection timing of -160 CAD aTDC. It was found that the model misfired for some of the cycles and the ignition was significantly advanced for the rest of the cycles. The higher pressure and heat release resulted due to the residuals from previous cycles. The evaluation of SKM2 at SOI_2 of -50 CAD aTDC can be seen in Figure 6(b). It can be seen that even though autoignition is happening

earlier than the experiments, lower pressure and heat release is observed in the model, showing that SKM2 is not able to accurately capture the chemistry at this operating condition. Figure 6(c) shows the results at SOI_2 of -35 CAD aTDC using SKM2. It can be seen that the autoignition is advanced for this operating condition as well. The pressure and heat release are lower as compared to the experiments and the two peaks in heat release profile are still present in SKM2 as well for this operating condition. Compared to SKM1, SKM2 has even lower pressure and heat release for the current operating condition. From the plots seen above, it can be concluded that SKM2 does not accurately capture the chemistry for any of the operating conditions for Double DI PFS combustion strategy.

Figure 7(a) shows the results for the second injection timing of -160 CAD aTDC using SKM3. SKM3 is showing very good agreement with the experimental pressure and heat release plots. It is also able to capture the cycle to cycle variability in the experiments similar to SKM1. The performance of SKM3 for second injection timing of -50 CAD aTDC can be seen in Figure 7(b). The agreement between the model and experiments is very good. SKM3 is able to predict start of autoignition with fair amount of accuracy and the pressure and heat release rate profile are also very close to the experiments. Hence, SKM3 is giving good results for moderately stratified mixture. Figure 7(c) shows the
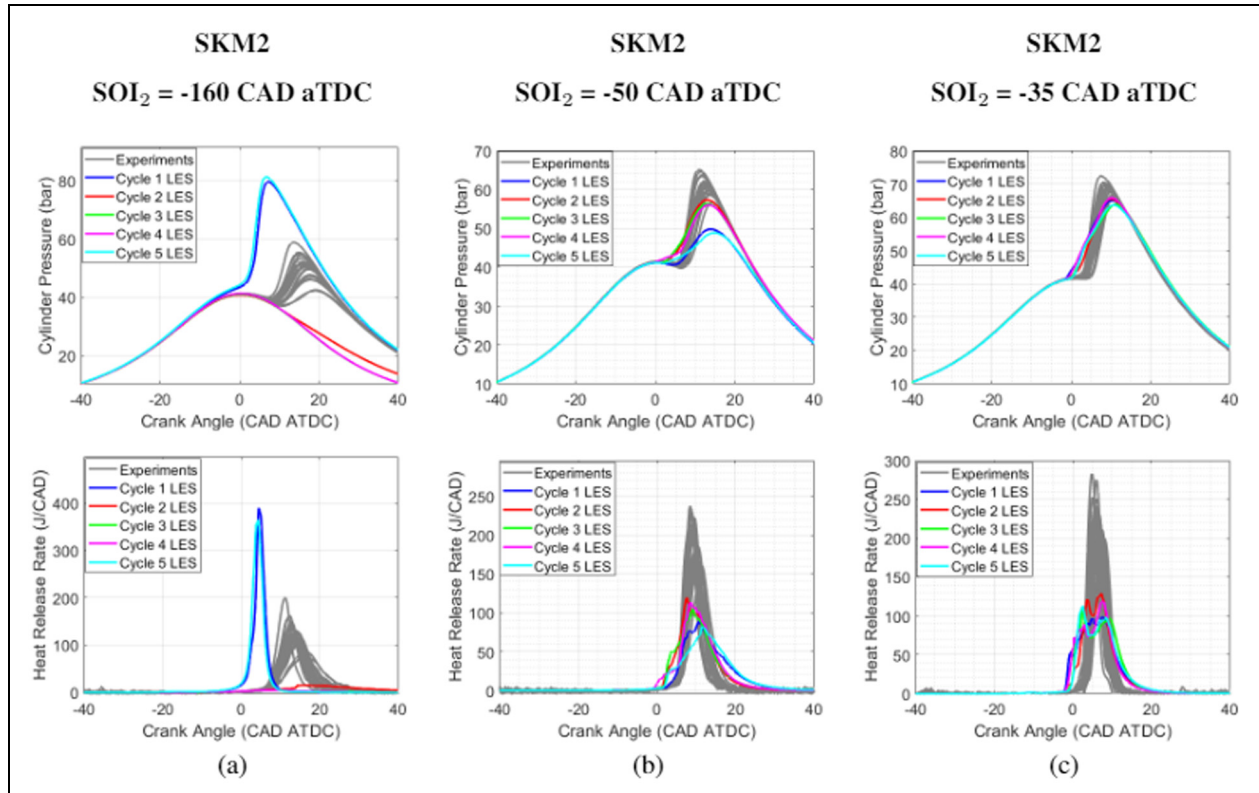
Figure 6. CFD results with SKM2. In-cylinder pressure (top) and HRR (bottom) are plotted for 20 consecutive experimental cycles (gray) and five consecutive LES cycles (colored) at $SOI_2 = -160$ CAD aTDC (a), $SOI_2 = -50$ CAD aTDC (b), and $SOI_2 = -35$ CAD aTDC (c).
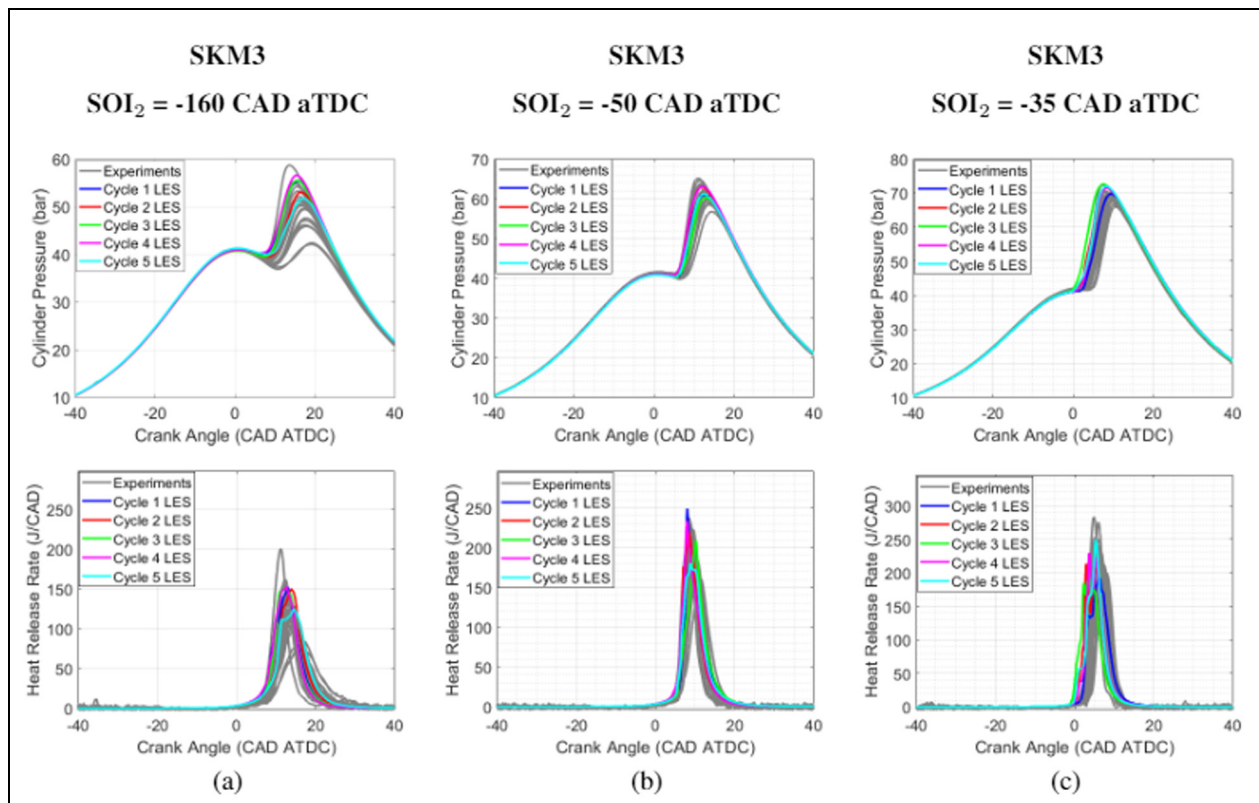
Figure 7. CFD results with SKM3. In-cylinder pressure (top) and HRR (bottom) are plotted for 20 consecutive experimental cycles (gray) and five consecutive LES cycles (colored) at $SOI_2 = -160$ CAD aTDC (a), $SOI_2 = -50$ CAD aTDC (b), and $SOI_2 = -35$ CAD aTDC (c).

comparison of pressure and heat release profiles for second injection timing of −35 CAD aTDC using SKM3. As discussed previously, $SOI_2 = -35$ CAD aTDC introduced highest stratification in the mixture from the currently studied experimental data set. It can be observed that SKM3 predicts autoignition a little earlier than the experiments, but overall, it shows good agreement with the pressure and heat release profiles of experiments. SKM3 is also predicting much higher heat release than SKM1 and SKM2, which was where the above discussed mechanisms struggled the most. Overall, SKM3 does a very good job at predicting the combustion for all three operating conditions.

The model evaluation for low, medium, and high stratification operating conditions shows that SKM1 works well for low to medium stratified conditions and struggles at highly stratified conditions. SKM2 is not predicting combustion accurately for any of the operating conditions. SKM3 on the other hand is accurately predicting start of autoignition as well as combustion progression and therefore has been used for further analysis of partial fuel stratification at second injection timings of −160, −50, and −35 CAD aTDC.

Analysis of the effects of stratification on the combustion using SKM3

Figure 8 shows the effect of compositional stratification on the combustion phasing for the second injection timing of −160, −50, and −35 CAD aTDC by plotting the joint probability density function (PDF) of temperature and atomic equivalence ratio in the combustion chamber at five (5) different crank angles of −10 CAD aTDC, TDC, CA10, CA50, and CA90 for each operating condition with SKM3. The figure was obtained by binning the cells of the combustion chamber into regions of ϕ of size 0.01 and plotting them against the mass-weighted average temperature of each region. The yellow dots on the plot each represent these individual zones at a specific temperature and equivalence ratio. The left column shows the joint PDF plots for $SOI_2 = -160$ CAD aTDC, the center column shows them for $SOI_2 = -50$ CAD aTDC, and the right column shows them for $SOI_2 = -35$ CAD aTDC.

It can be observed that at −10 CAD aTDC, the $SOI_2 = -160$ CAD aTDC case has low ϕ stratification in the combustion chamber as most of the mass is between the ϕ range of 0.2–0.6. For $SOI_2 = -50$ CAD aTDC case, there is moderate ϕ stratification at −10 CAD aTDC as shown by the tail end of the plot where some regions are at a higher ϕ of around 0.98. A significant amount of mass is still between ϕ range of 0.2–0.6. For the $SOI_2 = -35$ CAD aTDC case, high ϕ stratification is observed as some regions in the mixture reach a ϕ value of around 1.2. A significant amount of mass is still between ϕ range of 0.2–0.6 for this case as well. The effect of evaporative cooling can also be

verified as the gradient between the ϕ and the temperature is negative for all three cases.

The joint PDFs for the three operating conditions at TDC are shown in the second row. The ignition has started for $SOI_2 = -35$ CAD aTDC which has a highly stratified mixture in the cylinder. The richer regions have attained temperature similar to the leaner regions likely due to some exothermicity, suggesting that the richer regions might show low-temperature heat release (LTHR). As the mixture temperature is rising, the combustion starts from the richer regions as seen from the upper end of the tail and moves to higher temperatures as heat release progresses. For the $SOI_2 = -50$ CAD aTDC case, due to mixing, the number of regions having ϕ of around 1.0 have reduced and the ignition has not yet started. The $SOI_2 = -160$ CAD aTDC case shows an increase in mixture temperature due to compression but there has not been any significant change in ϕ distribution. The ignition has not started for this case as well. It can also be observed that the ignition started earlier for the highly stratified case due to the presence of higher number of richer zones, which supplements the experimental studies done on PFS. This effect can be used to advance the autoignition and control heat release and pressure rise rates.

The third row compares the joint PDFs at the corresponding CA10 value for all three operating conditions. The progression of combustion from the richest to the leanest regions can be observed for all the three cases. For $SOI_2 = -160$ CAD aTDC, it can be seen that the ϕ regions of 0.4–0.5 are dictating the CA10. The sequential autoignition of regions between ϕ of 0.6–0.8 is determining the CA10 for $SOI_2 = -50$ CAD aTDC case. CA10 for the $SOI_2 = -35$ CAD aTDC case is governed by the sequential autoignition of regions having $\phi > 0.7$. The plots also show that the richest regions that lead to ignition in the $SOI_2 = -50$ CAD aTDC and $SOI_2 = -35$ CAD aTDC cases have lower mass in the mixture compared the leaner regions.

The fourth row of plots show the joint PDFs at the corresponding CA50 value for all three operating conditions. The positive gradient between the ϕ and temperature in all the plots show the progression of combustion from the richest to the leanest regions as more of the mixture is burnt. It can also be seen that the CA50 has been advanced from 12.75 to 5.5 CAD aTDC as the second injection is delayed from −160 to −35 CAD aTDC. The difference in ϕ stratification results in different burnt gas temperatures. The $SOI_2 = -160$ CAD aTDC case reaches burnt gas temperatures of around 2100 K. The burnt gas temperatures for the moderately ($SOI_2 = -50$ CAD aTDC) and highly stratified cases ($SOI_2 = -35$ CAD aTDC) are 2400 and 2700 K. Burnt gas temperatures are higher than the NO_x formation threshold of 1800 K, however lower mass of the richer regions alleviates the NO_x formation. However, there will be an increase in NO_x formation as the SOI_2 is retarded. For $SOI_2 = -160$ CAD
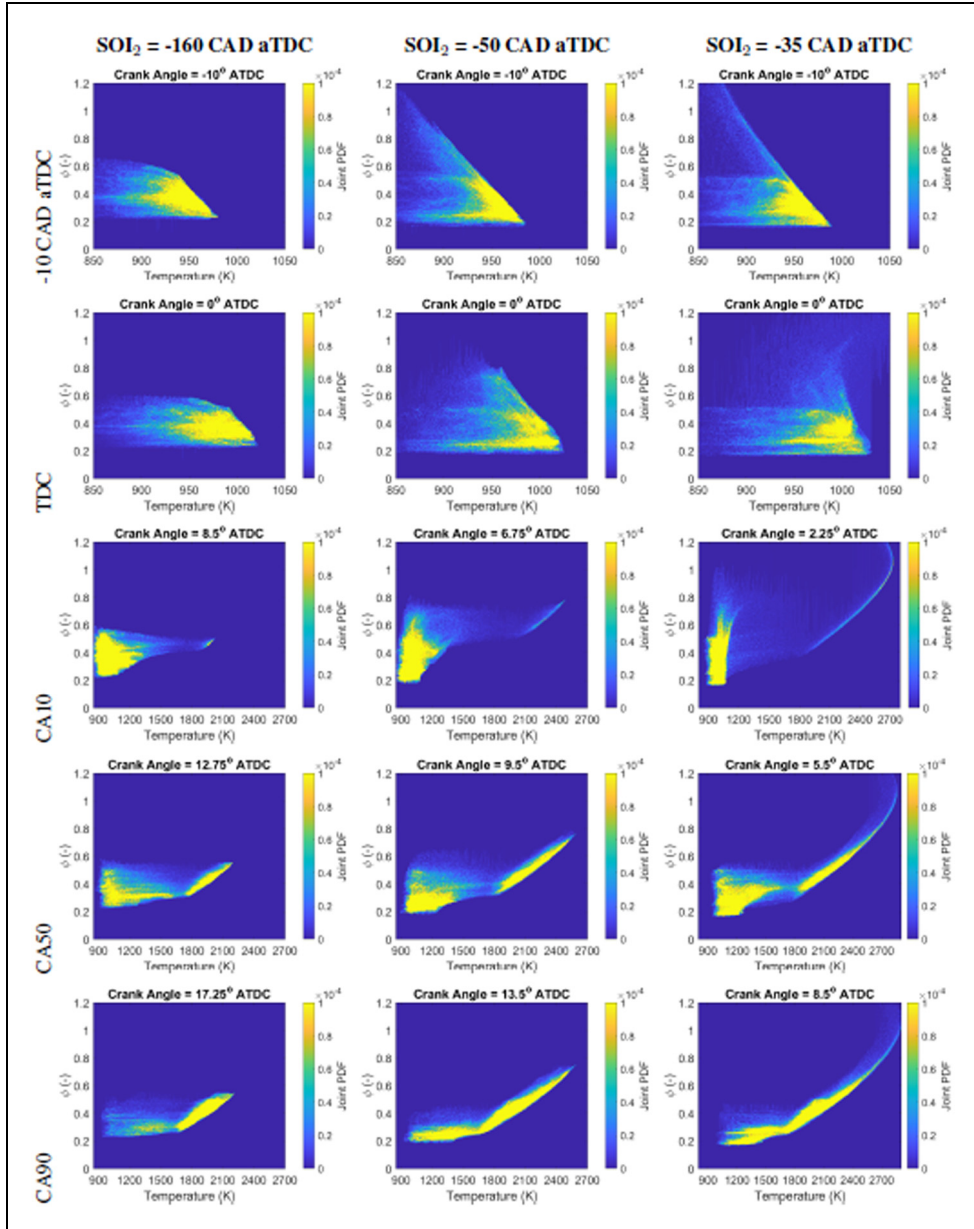
Figure 8. Contours of the joint PDF of mass as a function of equivalence ratio and temperature in the combustion chamber at -10 CAD aTDC, TDC, CA10, CA50, and CA90 for the fifth modeled cycle with $SOI_2 = -160$ CAD aTDC (left), $SOI_2 = -50$ CAD aTDC (center), and $SOI_2 = -35$ CAD aTDC (right). SKM3 was used in the simulations.

aTDC, the CA50 is determined by zones having ϕ between 0.3 and 0.5. The sequential autoignition of regions between ϕ of 0.4 and 0.6 is determining the CA50 for $SOI_2 = -50$ CAD aTDC case. CA50 for the $SOI_2 = -35$ CAD aTDC case is governed by the sequential autoignition of regions having ϕ between 0.4 and 0.7. The last row compares the joint PDFs at the corresponding CA90 value for all three operating conditions. The sequential autoignition of regions between ϕ of 0.2 and 0.3 is determining the CA90 for $SOI_2 = -160$ CAD aTDC case. For second injection timings of -50 and -35 CAD aTDC, the CA90 is dictated by regions having a ϕ range of 0.25–0.40.
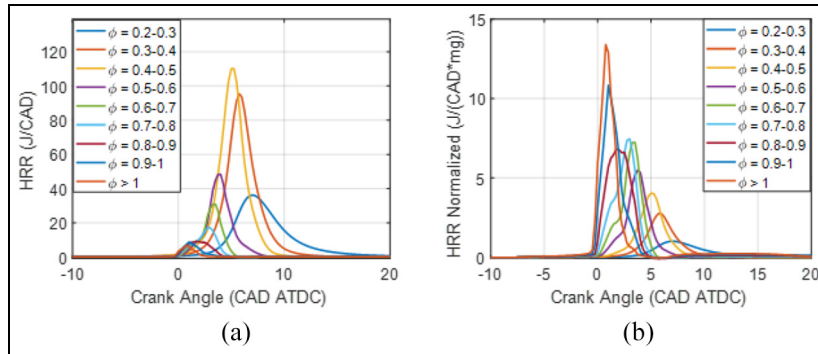
Figure 9 shows the heat release of different regions of ϕ in the combustion chamber (left) and the normalized heat release rate corresponding to those regions for $SOI_2 = -160$ CAD aTDC case using SKM3. The heat release was normalized using the mass of each region and the binning size was ϕ of 0.1. Interestingly, the heat release starts with the 0.4–0.5 region, which means that the richer ϕ s are not the most reactive regions in the chamber due to the competition between thermal stratification and the ϕ-sensitivity of the fuel. If the temperature of the richer regions is too low, the ϕ-sensitivity cannot overcome the thermal effect and the ignition will be dictated by intermediate ϕ s. Total
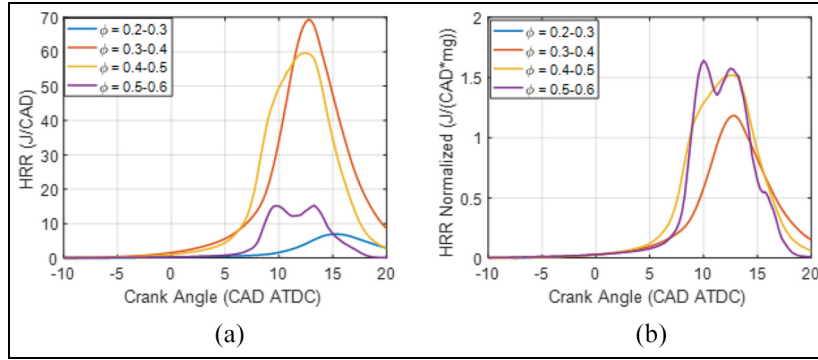
Figure 9. Heat release rates for four zones of different ϕ in the combustion chamber for the fifth modeled cycle at $SOI_2 = -160$ CAD aTDC using SKM3. (a) Absolute HRR and (b) HRR normalized by the mass of each zone.
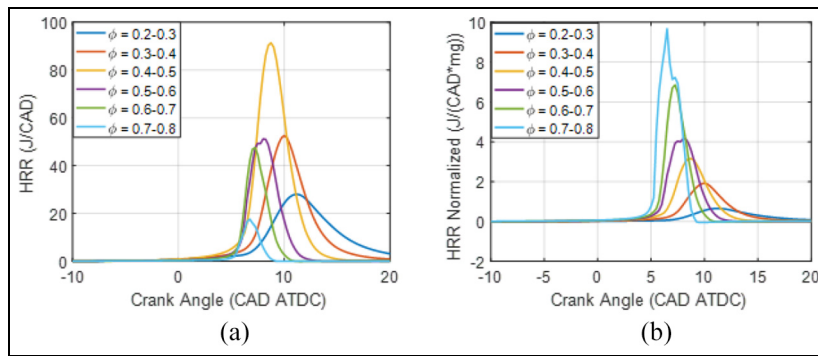
Figure 10. Heat release rates for four zones of different ϕ in the combustion chamber for the fifth modeled cycle at $SOI_2 = -50$ CAD aTDC using SKM3. (a) Absolute HRR and (b) HRR normalized by the mass of each zone.


Figure 11. Heat release rates for four zones of different ϕ in the combustion chamber for the fifth modeled cycle at $SOI_2 = -35$ CAD aTDC using SKM3. (a) Absolute HRR and (b) HRR normalized by the mass of each zone.

heat release depends on the mass of each region therefore most of the heat release for this case occurs from regions between ϕ of 0.3 and 0.5.

Figure 10 shows the heat release of different regions of ϕ in the combustion chamber (left) and the normalized heat release rate corresponding to those regions for $SOI_2 = -50$ CAD aTDC case using SKM3. The richest region of $\phi = 0.7-0.8$ ignites first and sequential auto ignition of leaner regions follows. As seen from the heat release plot, the majority of the heat is released by the regions that account for the bulk of the mass found in

the mixture. In this case, the regions of ϕ between 0.3 and 0.7 contribute the most toward heat release. The $SOI_2 = -35$ CAD aTDC case, shows sequential auto-ignition most prominently in Figure 11, which shows the heat release of different regions of ϕ in the combustion chamber and the normalized heat release rate corresponding to those regions. The delayed second injection results in higher ϕ stratification due to which higher number of bins have been used in this figure. As seen in the normalized heat release rate plot, the ignition once again starts with cells which have $\phi > 1$ in
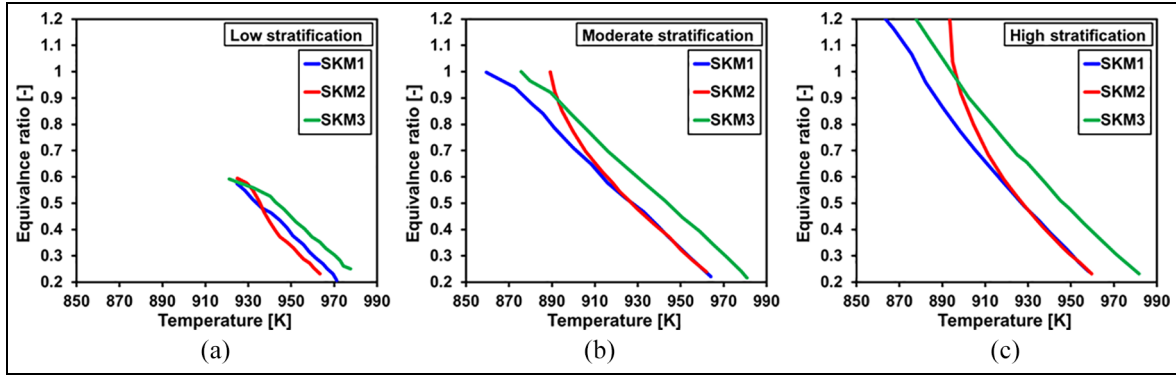
Figure 12. ϕ-temperature distribution in the cylinder from CFD for low (a), moderate (b), and high (c) stratification using SKM1 (blue), SKM2 (red), and SKM3 (green).
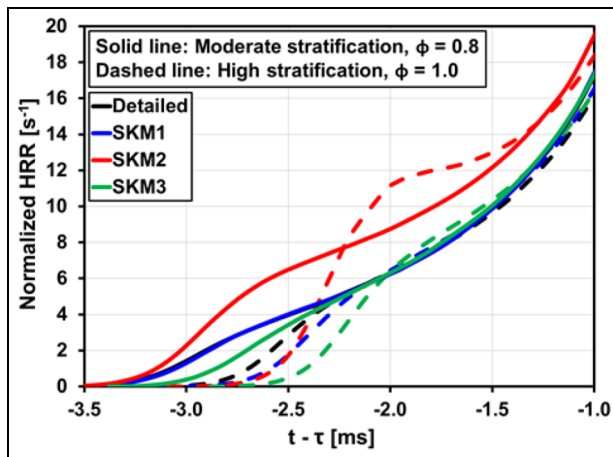
Figure 13. HRR normalized by the total heat released versus time relative to the ignition delay ($t-\tau$) at the ϕ of ignition for moderate (solid lines, $\phi = 0.8$) and high (dashed lines, $\phi = 1.0$) stratification using the detailed mechanism (black), SKM1 (blue), SKM2 (red), and SKM3 (green).

the combustion chamber and subsequently, it progresses to the leaner regions. Most of the heat release at this operating condition, is contributed by the regions having ϕ of 0.3–0.6. As seen in the CDF plot earlier (Figure 3), around 10% of the total mass is at a $\phi > 0.6$. This shows that even though the richer regions are starting the ignition, they get consumed very fast. Figures 10 and 11 also show that the ϕ regions of 0.2–0.3 are burning more slowly than the richer regions, which can result in better control of the heat release for moderate and highly stratified cases.

## Chemical kinetic analysis of SKM1, SKM2, and SKM3

Chemical kinetic simulations are carried out in CHEMKIN to understand the performance of SKM1, SKM2, and SKM3 in the CFD simulations. The joint PDF of temperature and equivalence ratio in the combustion chamber at -10 CAD aTDC (which is shown

in Figure 8 for SKM3 and in Appendix A for SKM1 and SKM2) is used to generate a ϕ-temperature distribution that represents the in-cylinder reactivity at the time of ignition. Data at -10 CAD aTDC are selected because there is not noticeable experimental heat release at this crank angle. For simplicity, only the highest temperature value at a given ϕ is simulated, which is representative of the most reactive temperature at each ϕ. The resulting temperature versus ϕ distributions for the various SOI$_2$ are imposed in a closed, homogeneous, constant-volume reactor in CHEMKIN to obtain an ignition delay value (τ) for each ϕ-T combination. CHEMKIN simulations are performed with SKM1, SKM2, SKM3, and the detailed chemical kinetic mechanism from LLNL used to generate the skeletal mechanisms.

Figure 12 shows the ϕ-temperature distributions for the various levels of stratification: low (a), moderate (b) and high (c); and for SKM1 (blue), SKM2 (red), and SKM3 (green). The ϕ-temperature distribution at a given level of stratification is not the same for all the mechanisms because of the differences in IVC temperature (see Figure 4). Interestingly, the slope of the ϕ-temperature distribution of SKM2 for moderate and high stratification changes at $\phi = 0.6$. This is because the regions richer than $\phi = 0.6$ show LTHR in the CFD simulations with SKM2, which increases the in-cylinder local temperature and pressure. Note that SKM1 and SKM3 do not show this behavior. To better illustrate this point, Figure 13 shows the pre-ignition HRR at the ϕ of ignition for moderate stratification (solid lines, $\phi = 0.8$) and high stratification (dashed lines, $\phi = 1.0$) obtained in CHEMKIN with the detailed mechanism (black), SKM1 (blue), SKM2 (red), and SKM3 (green). SKM2 shows a higher early HRR than the other mechanisms, which implies that it releases more heat during the pre-ignition than the detailed mechanism, SKM1, and SKM3. This might affect the sequential autoignition of the CFD simulations, which might be one of the reasons for the poor performance of SKM2.

Figure 14 shows the ignition delay distribution that corresponds to each ϕ-temperature distribution shown
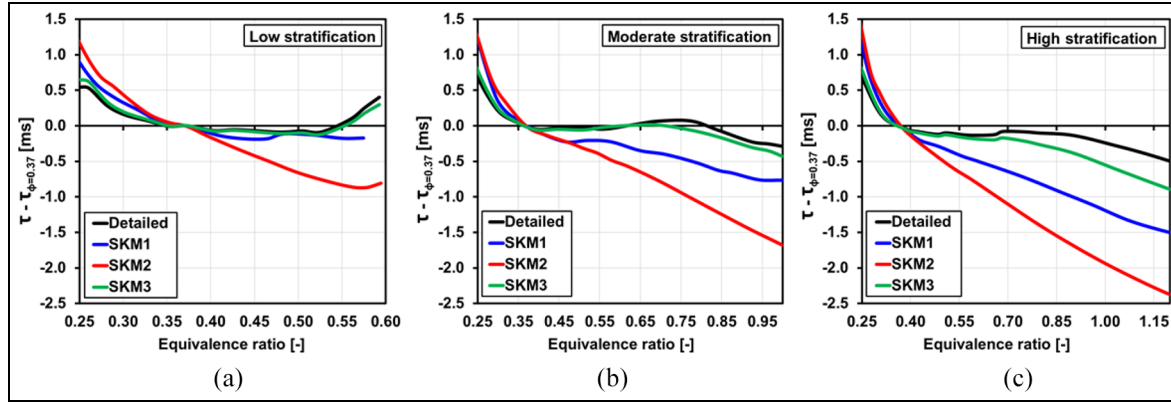
Figure 14. Ignition delay distribution that corresponds to each ϕ-temperature distribution shown in Figure 12 for low (a), moderate (b), and high (c) stratification using the detailed mechanism (black), SKM1 (blue), SKM2 (red), and SKM3 (green).

in Figure 12 obtained with the detailed mechanism (black), SKM1 (blue), SKM2 (red), and SKM3 (green). The pressure used in the simulations is equal to 35.4 bar, which corresponds to the experimental in-cylinder pressure at -10 CAD aTDC. The ϕ-temperature distribution used for the detailed mechanism was obtained by scaling the ϕ-temperature distribution of SKM1 with the IVC temperature ratio between the experiments and the CFD simulations with SKM1 (ϕ-$T_{Detailed} = \phi$-$T_{SKM1} \cdot T_{IVCexp.} / T_{IVCSKM1}$). This approach was also applied to the ϕ-temperature distribution of SKM3 obtaining very consistent results ans showing that the in-cylinder ϕ-temperature distribution is scalable with the IVC temperature ratio. The change in ignition delay relative to $\phi = 0.37$ ($\tau - \tau_{\phi = 0.37}$), which is the global ϕ of the experiments, is used in the plot. This relative variation in ignition delay represents the potential spread in ignition delay for a stratified charge, since the ignition delay of $\phi = 0.37$ represents the reactivity under homogeneous conditions. First, shorter ignition delays than $\phi = 0.37$ would advance the ignition. Second, the spread of ignition delays (difference between the shortest and the longest ignition delay within the ignition delay distribution) would spread the heat release compared to that of homogeneous conditions, with the amount depending on the amount of fuel at each ϕ within the stratified charge. The deviation between the detailed mechanism and the skeletal mechanisms is used to explain the performance of the skeletal mechanisms in CFD, assuming that the detailed mechanism is reasonably accurate.

SKM1 shows a good agreement with the detailed mechanism at low levels of stratification. However, the ignition of the richer regions progressively becomes overly advanced as the level of stratification increases. Thus, SKM1 predicts earlier ignition than the detailed mechanism at moderate and high stratification. This is in good agreement with the CFD results shown in Figures 4 and 5. SKM1 also shows a higher spread of ignition delays than the detailed mechanism for moderate and high stratification, which suggests a higher

spread of heat release in the CFD simulations at these conditions. This is also in good agreement with with the CFD results of Figure 5(b) and (c), in which SKM1 shows lower peaks of HRR than the experiments.

SKM2 shows shorter ignition delays relative to $\phi = 0.37$ and much higher spread of ignition delays than the detailed mechanism for the three levels of stratification. This might explain why SKM2 predicts more advanced ignitions and lower peaks of HRR than those of the experiments (see Figure 6(b) and (c)). The high spread of ignition delays of SKM2 will lead to overly high spread of heat release in the CFD simulations, that might result into misfires at low levels of stratification as shown in Figure 6(a). Note that the low stratified point has higher propensity to misfires than the other conditions due to the more retarded CA50 and the higher cycle-to-cycle variation (experimental CA50 and COV-IMEP$_g$ for the low stratified point are equal to 14.0 CAD aTDC and 3.2%, respectively).

Finally, SKM3 shows the best agreement with the detailed mechanism among all the skeletal mechanisms, which suggests that SKM3 is more accurate than SKM1 and SKM2. The largest deviation between SKM3 and the detailed mechanism occurs for high stratification. SKM3 shows slightly shorter ignition delays relative to $\phi = 0.37$ than the detailed mechanism at this condition, which might explain why the CFD simulations predict a slightly more advanced ignition point than the experiments (as shown in Figure 7(c)). Nevertheless, this deviation is within the experimental repeatability and SKM3 shows a very good performance for the conditions tested in this investigation.

Summary and conclusions

The present study used a 3D CFD model with Large Eddy Simulations to simulate the partial fuel stratification using research grade gasoline under moderate boosting. A split injection strategy was used where 80% of the fuel is injected at -300 CAD aTDC and the remaining 20% of the fuel is injected during the second

injection. The timing of second injection is varied from -160 CAD to -35 CAD aTDC to change the ϕ stratification in the cylinder. The model was validated using three (3) different chemical kinetic mechanisms at three (3) different operating conditions. The modeling results were used to analyze the performance of the mechanisms and to recommend the mechanism that can be used in the widest variety of operating conditions.

- SKM1 provided acceptable agreement with the experimental results for second injection timings of -160 and -50 CAD aTDC. SKM1 did not predict autoignition and combustion progression accurately for $SOI_2 = -35$ CAD aTDC case.
- SKM2 did not perform well for all three operating conditions. The model had misfires at $SOI_2 = -160$ CAD aTDC and early ignition and overly slow heat release at second injection timings of -50 and -35 CAD aTDC. Chemical kinetic simulations suggest that this might be because SKM2 leads to an overly wide ignition delay variation from the richest to the leanest regions.
- SKM3 showed very good agreement with the experiments for all three operating conditions. The combustion was predicted a little earlier for $SOI_2 = -35$ CAD aTDC case, but overall heat release and combustion duration was very accurately predicted.
- SKM3 is the recommended mechanism for different ranges of operating conditions for PFS modeling using research grade gasoline.
- Second injection timing has a significant impact on ϕ stratification of the mixture. $SOI_2 = -160$ CAD aTDC case showed ϕ ranging from 0.2 to 0.6. $SOI_2 = -50$ CAD aTDC case showed moderate stratification with ϕ ranging from 0.18 to 0.80. The local ϕ varied from 0.15 to 1.02 for $SOI_2 = -35$ CAD aTDC.
- For moderate and high levels of stratification, the richer regions in the mixture ignite first and the sequential autoignition of leaner regions follows. However, ignition starts at intermediate ϕ s for low levels of stratification because the thermal stratification overcomes the ϕ-sensitivity of the fuel at this condition.
- The ϕ regions with higher mass contribute more to the heat release even if they are leaner comparatively.

Declaration of conflicting interests

Funding

ORCID iDs

Gaurav Guleria 🔘 https://orcid.org/0000-0002-7258-8419
Dimitris Assanis 🔘 https://orcid.org/0000-0001-5506-806X

References

1. Najt PM and Foster DE. Compression-ignited homogeneous charge combustion. *SAE Trans* 1983; 92: 964–979.
2. Thring RH. Homogeneous-charge compression-ignition (HCCI) engines. *SAE technical paper* 892068, 1989.
3. Onishi S, Jo SH, Shoda K, Jo PD and Kato S. Active thermo-atmosphere combustion (ATAC)—a new combustion process for internal combustion engines. *SAE Trans* 1979; 88: 1851–1860.
4. Stanglmaier RH and Roberts CE. Homogeneous charge compression ignition (HCCI): benefits, compromises, and future engine applications. *SAE Trans* 1999; 108: 2138–2145.
5. Snyder J, Dronniou N, Dec J and Hanson R. PLIF measurements of thermal stratification in an HCCI engine under fired operation. *SAE Int J Engines* 2011; 4(1): 1669–1688.
6. Zigler BT, Walton SM, Karwat DM, Assanis D, Wooldridge MS and Wooldridge ST. A multi-axis imaging study of spark-assisted homogeneous charge compression ignition phenomena in a single-cylinder research engine. In: *Internal combustion engine division fall technical conference*, 14–17 October 2007, Charleston, SC, vol. 48116, pp.395–405. New York, NY: American Society of Mechanical Engineers.
7. Zigler BT, Walton SM, Assanis D, Perez E, Wooldridge MS and Wooldridge ST. An imaging study of compression ignition phenomena of iso-octane, indolene, and gasoline fuels in a single-cylinder research engine. *J Eng Gas Turbine Power* 2008; 130(5): 052803.
8. Sjöberg M, Dec JE and Hwang W. Thermodynamic and chemical effects of EGR and its constituents on HCCI autoignition. *SAE Trans* 2007; 116: 271–289.
9. Shi L, Cui Y, Deng K, Peng H and Chen Y. Study of low emission homogeneous charge compression ignition (HCCI) engine using combined internal and external exhaust gas recirculation (EGR). *Energy* 2006; 31(14): 2665–2676.
10. Olsson JO, Tunestål P, Ulfvik J and and Johansson B. The effect of cooled EGR on emissions and performance of a turbocharged HCCI engine. SAE technical paper 2003-01-0743, 2003.
11. Christensen M and Johansson B. Supercharged homogeneous charge compression ignition (HCCI) with exhaust gas recirculation and pilot fuel. SAE technical paper 2000-01-1835, 2000.
12. Yao M, Zheng Z and Liu H. Progress and recent trends in homogeneous charge compression ignition (HCCI) engines. *Prog Energy Combust Sci* 2009; 35(5): 398–437.
13. Cairns A and Blaxill H. The effects of combined internal and external exhaust gas recirculation on gasoline

controlled auto-ignition. SAE technical paper 2005-01-0133, 2005.

14. Christensen M, Hultqvist A and Johansson B. Demonstrating the multi fuel capability of a homogeneous charge compression ignition engine with variable compression ratio. *SAE Trans* 1999; 108: 2099–2113.

15. Hyvönen J, Haraldsson G and Johansson B. Operating conditions using spark assisted HCCI combustion during combustion mode transfer to SI in a multi-cylinder VCR-HCCI engine. SAE technical paper 2005-01-0109, 2005.

16. Haraldsson G, Tunestål P, Johansson B and Hyvönen J. HCCI combustion phasing in a multi cylinder engine using variable compression ratio. *SAE Trans* 2002; 111: 2654–2663.

17. Hyvönen J, Haraldsson G and Johansson B. Operating range in a multi cylinder HCCI engine using variable compression ratio. *SAE Trans* 2003; 112: 1222–1232.

18. Triantopoulos V, Bohac S, Martz J, et al. The effect of EGR dilution on the heat release rates in boosted spark-assisted compression ignition (SACI) engines. *SAE Int J Adv Curr Pract Mobil* 2020; 2(4): 2183–2195.

19. Zigler BT, Keros PE, Helleberg KB, Fatouraie M, Assanis D and Wooldridge MS. An experimental investigation of the sensitivity of the ignition and combustion properties of a single-cylinder research engine to spark-assisted HCCI. *Int J Engine Res* 2011; 12(4): 353–375.

20. Triantopoulos V, Martz JB, Sterniak J, Lavoie G, Assanis DN and Bohac SV. Operating limits of spark-assisted compression ignition combustion under boosted ultra-EGR dilute conditions in a negative valve overlap engine. In: *Internal combustion engine division fall technical conference*, 20–23 October 2019, Chicago, IL, vol. 59346, p.V001T03A013. New York, NY: American Society of Mechanical Engineers.

21. Gerow MS, Shingne PS, Triantopoulos V, Bohac SV and Martz JB. A comparison of valving strategies appropriate for multimode combustion within a downsized boosted automotive engine part II: mid load operation within the SACI combustion regime. *J Eng Gas Turbine Power* 2014; 136(10): 101508.

22. Olsson JO, Tunestål P and Johansson B. Boosting for high load HCCI. *SAE Trans* 2004; 113: 579–588.

23. Dec JE and Yang Y. Boosted HCCI for high power without engine knock and with ultra-low NOx emissions-using conventional gasoline. *SAE Int J Engines* 2010; 3(1): 750–767.

24. Yap D, Wyszynski ML, Megaritis A and Xu H. Applying boosting to gasoline HCCI operation with residual gas trapping. SAE technical paper 2005-01-2121, 2005.

25. Mamalis S, Nair V, Andruskiewicz P, et al. Comparison of different boosting strategies for homogeneous charge compression ignition engines-a modeling study. *SAE Int J Engines* 2010; 3(1): 296–308.

26. Sjöberg M and Dec JE. EGR and intake boost for managing HCCI low-temperature heat release over wide ranges of engine speed. *SAE Trans* 2007; 116: 65–77.

27. Mamalis S, Babajimopoulos A, Guralp O, Najt PM and Assanis DN. The interaction between compression ratio, boosting and variable valve actuation for high load homogeneous charge compression ignition: a modeling study. *Int J Engine Res* 2014; 15(4): 460–470.

28. Sjöberg M, Dec JE, Babajimopoulos A and Assanis D. Comparing enhanced natural thermal stratification against retarded combustion phasing for smoothing of HCCI heat-release rates. *SAE Trans* 2004; 113: 1557–1575.

29. Sjöberg M, Dec JE and Cernansky NP. Potential of thermal stratification and combustion retard for reducing pressure-rise rates in HCCI engines, based on multi-zone modeling and experiments. *SAE Trans* 2005; 114: 236–251.

30. Sjöberg M and Dec JE. Smoothing hcci heat release with vaporization-cooling-induced thermal stratification using ethanol. *SAE Int J Fuels Lubr* 2012; 5(1): 7–27.

31. Dempsey AB, Curran SJ and Wagner RM. A perspective on the range of gasoline compression ignition combustion strategies for high engine efficiency and low NOx and soot emissions: effects of in-cylinder fuel stratification. *Int J Engine Res* 2016; 17(8): 897–917.

32. Aoyama T, Hattori Y, Mizuta J and Sato Y. An experimental study on premixed-charge compression ignition gasoline engine. *SAE technical paper* 960081, 1996.

33. Kanda T, Hakozaki T, Uchimoto T, Hatano J, Kitayama N and Sono H. PCCI operation with early injection of conventional diesel fuel. *SAE Trans* 2005; 114: 584–593.

34. Kokjohn SL, Hanson RM, Splitter DA and Reitz RD. Experiments and modeling of dual-fuel HCCI and PCCI combustion using in-cylinder fuel blending. *SAE Int J Engines* 2010; 2(2): 24–39.

35. Hanson RM, Kokjohn SL, Splitter DA and Reitz RD. An experimental investigation of fuel reactivity controlled PCCI combustion in a heavy-duty engine. *SAE Int J Engines* 2010; 3(1): 700–716.

36. Splitter D, Kokjohn S, Rein K, Hanson R, Sanders S and Reitz R. An optical investigation of ignition processes in fuel reactivity controlled PCCI combustion. *SAE Int J Engines* 2010; 3(1): 142–162.

37. Kook S and Bae C. Combustion control using two-stage diesel fuel injection in a single-cylinder PCCI engine. *SAE Trans* 2004; 113: 563–578.

38. Kokjohn SL, Hanson RM, Splitter DA and Reitz RD. Fuel reactivity controlled compression ignition (RCCI): a pathway to controlled high-efficiency clean combustion. *Int J Engine Res* 2011; 12(3): 209–226.

39. Kokjohn S, Hanson R, Splitter D, Kaddatz J and Reitz R. Fuel reactivity controlled compression ignition (RCCI) combustion in light-and heavy-duty engines. *SAE Int J Engines* 2011; 4(1): 360–374.

40. Splitter D, Hanson R, Kokjohn S and Reitz RD. Reactivity controlled compression ignition (RCCI) heavy-duty engine operation at mid-and high-loads with conventional and alternative fuels. SAE technical paper 2011-01-0363, 2011.

41. Nieman DE, Dempsey AB and Reitz RD. Heavy-duty RCCI operation using natural gas and diesel. *SAE Int J Engines* 2012; 5(2): 270–285.

42. Sellnau M, Sinnamon J, Hoyer K and Husted H. Gasoline direct injection compression ignition (GDCI)-diesel-like efficiency with low CO$_2$ emissions. *SAE Int J Engines* 2011; 4(1): 2010–2022.

43. Sellnau MC, Sinnamon J, Hoyer K and Husted H. Full-time gasoline direct-injection compression ignition (GDCI) for high efficiency and low NOx and PM. *SAE Int J Engines* 2012; 5(2): 300–314.

44. Kolodziej C, Kodavasal J, Ciatti S, Som S, Shidore N and Delhom J. Achieving stable engine operation of gasoline compression ignition using 87 AKI gasoline down to idle. SAE technical paper 2015-01-0832, 2015.

45. Kodavasal J, Kolodziej CP, Ciatti SA and Som S. Computational fluid dynamics simulation of gasoline compression ignition. *J Energy Resour Technol* 2015; 137(3): 032212.

46. Sjöberg M and Dec JE. Smoothing HCCI heat-release rates using partial fuel stratification with two-stage ignition fuels. *SAE Trans* 2006; 115: 318–334.

47. Dec JE, Yang Y and Dronniou N. Boosted HCCI-controlling pressure-rise rates for performance improvements using partial fuel stratification with conventional gasoline. *SAE Int J Engines* 2011; 4(1): 1169–1189.

48. Yang Y, Dec J, Dronniou N, Sjöberg M and Cannella W. Partial fuel stratification to control HCCI heat release rates: fuel composition and other factors affecting pre-ignition reactions of two-stage ignition fuels. *SAE Int J Engines* 2011; 4(1): 1903–1920.

49. Yang Y, Dec JE, Dronniou N and Sjöberg M. Tailoring HCCI heat-release rates with partial fuel stratification: comparison of two-stage and single-stage-ignition fuels. *Proc Combust Inst* 2011; 33(2): 3047–3055.

50. Dernotte J, Dec J and Ji C. Efficiency improvement of boosted low-temperature gasoline combustion engines (LTGC) using a double direct-injection strategy. SAE technical paper 2017-01-0728, 2017.

51. Easley WL, Agarwal A and Lavoie GA. Modeling of HCCI combustion and emissions using detailed chemistry. *SAE Trans* 2001; 110: 1045–1061.

52. Aceves SM, Martinez-Frias J, Flowers DL, et al. A decoupled model of detailed fluid mechanics followed by detailed chemical kinetics for prediction of iso-octane HCCI combustion. *SAE Trans* 2001; 110: 2135–2146.

53. Fiveland SB and Assanis DN. Development and validation of a quasi-dimensional model for HCCI engine performance and emissions studies under turbocharged conditions. *SAE Trans* 2002; 111: 842–860.

54. Kong SC and Reitz RD. Use of detailed chemical kinetics to study HCCI engine combustion with consideration of turbulent mixing effects. *J Eng Gas Turbine Power* 2002; 124(3): 702–707.

55. Jia M and Xie M. A chemical kinetics model of iso-octane oxidation for HCCI engines. *Fuel* 2006; 85(17–18): 2593–2604.

56. Priyadarshini P, Sofianopoulos A, Mamalis S, Lawler B, Lopez-Pintor D and Dec JE. Understanding partial fuel stratification for low temperature gasoline combustion using large eddy simulations. *Int J Engine Res* 2021; 22: 1872–1887.

57. Dec JE, Yang Y, Dernotte J and Ji C. Effects of gasoline reactivity and ethanol content on boosted, premixed and partially stratified low-temperature gasoline combustion (LTGC). *SAE Int J Engines* 2015; 8(3): 935–955.

58. Lopez-Pintor D, Dec J and Gentz G. Experimental evaluation of a custom gasoline-like blend designed to simultaneously improve ϕ-sensitivity, ron and octane sensitivity. *SAE Int J Adv Curr Pract Mobil* 2020; 2(4): 2196–2216.

59. Ji C, Dec J, Dernotte J and Cannella W. Boosted premixed-LTGC/HCCI combustion of EHN-doped gasoline for engine speeds up to 2400 rpm. *SAE Int J Engines* 2016; 9(4): 2166–2184.

60. Gentz G, Dernotte J, Ji C, Lopez-Pintor D and Dec J. Combustion-timing control of low-temperature gasoline combustion (LTGC) engines by using double direct-injections to control kinetic rates. SAE technical paper 2019-01-1156, 2019.

61. Lopez-Pintor D, Gentz G and and Dec J. Mixture stratification for CA50 control of LTGC engines with reactivity-enhanced and non-additized gasoline. SAE technical paper 2021-01-0513, 2021.

62. Richards KJ, Senecal PK and Pomraning E. *Converge 2.4*. Madison, WI: Convergent Science, 2020.

63. Senecal PK, Richards KJ, Pomraning E, et al. A new parallel cut-cell cartesian CFD code for rapid grid generation applied to in-cylinder diesel engine simulations. SAE technical paper 2007-01-0159, 2007.

64. Dronniou N and Dec J. Investigating the development of thermal stratification from the near-wall regions to the bulk-gas in an hcci engine with planar imaging thermometry. *SAE Int J Engines* 2012; 5(3): 1046–1074.

65. Pomraning E. *Development of large eddy simulation turbulence models*. PhD Thesis, University of Wisconsin–Madison, USA, 2000.

66. Beale JC and Reitz RD. Modeling spray atomization with the Kelvin-Helmholtz/Rayleigh-Taylor hybrid model. *Atomization Spray* 1999; 9(6): 623–650.

67. Reitz RD. Mechanism of breakup of round liquid jets. In: Cheremisinoff NP (ed.) *Encyclopedia of fluid mechanics*. Vol. 3. Houston, TX: Gulf Publishing Company, 1986, pp.233–249.

68. Amsden AA and O'Rourke PJ, and T doi = 10.2172/6228444 Daniel Butler. KIVA-II: a computer program for chemically reactive flows with sprays. Technical report, Los Alamos National Lab. (LANL), USA, 1989.

69. Schmidt DP and Rutland CJ. A new droplet collision algorithm. *J Comput Phys* 2000; 164(1): 62–80.

70. O'Rourke PJ and Amsden AA. The tab method for numerical calculation of spray droplet breakup. *SAE technical paper* 872089, 1987.

71. O'Rourke PJ and Amsden AA. A spray/wall interaction submodel for the KIVA-3 wall film model. *SAE Trans* 2000; 109: 281–298.

72. Senecal PK, Pomraning E, Richards KJ, et al. Multi-dimensional modeling of direct-injection diesel spray liquid length and flame lift-off length using CFD and parallel detailed chemistry. *SAE Trans* 2003; 112(3): 1331–1351.

73. Babajimopoulos A, Assanis DN, Flowers DL, Aceves SM and Hessel RP. A fully coupled computational fluid dynamics and multi-zone model with detailed chemical kinetics for the simulation of premixed charge compression ignition engines. *Int J Engine Res* 2005; 6(5): 497–512.

74. Amsden AA and Findley M. KIVA-3V: A block-structured KIVA program for engines with vertical or canted valves. Report, Lawrence Livermore National Lab. (LLNL), USA, 1997.

75. Werner H and Wengle H. Large-eddy simulation of turbulent flow over and around a cube in a plate channel. In: Durst F, Friedrich R, Launder BE, Schmidt FW, Schumann U and Whitelaw JH (eds) *Turbulent shear flows 8*. Berlin, Heidelberg: Springer, 1993, pp.155–168.

76. Desantes JM, García-Oliver JM, Novella R, et al. Application of a coupled eulerian spray approach and a flamelet-based combustion model to single hole primary reference fuel sprays. In *21st annual conference on liquid atomization and spray systems (ILASS) – Asia*, Zhenjiang, China, 23–26 October 2020.

77. Mehl M, Zhang K, Wagnon S, et al. A comprehensive detailed kinetic mechanism for the simulation of transportation fuels. In: *10th US national combustion meeting*, College Park, MD, US, 23–26 April 2017.

78. Lopez-Pintor D, Dec J and Gentz G. ϕ–Sensitivity for LTGC engines: understanding the fundamentals and tailoring fuel blends to maximize this property. SAE techical paper 2019-01-0961, 2019.

Appendix A

Figures A1 and A2 show the joint probability density function (PDF) of temperature and equivalence ratio in the combustion chamber at five different crank angles
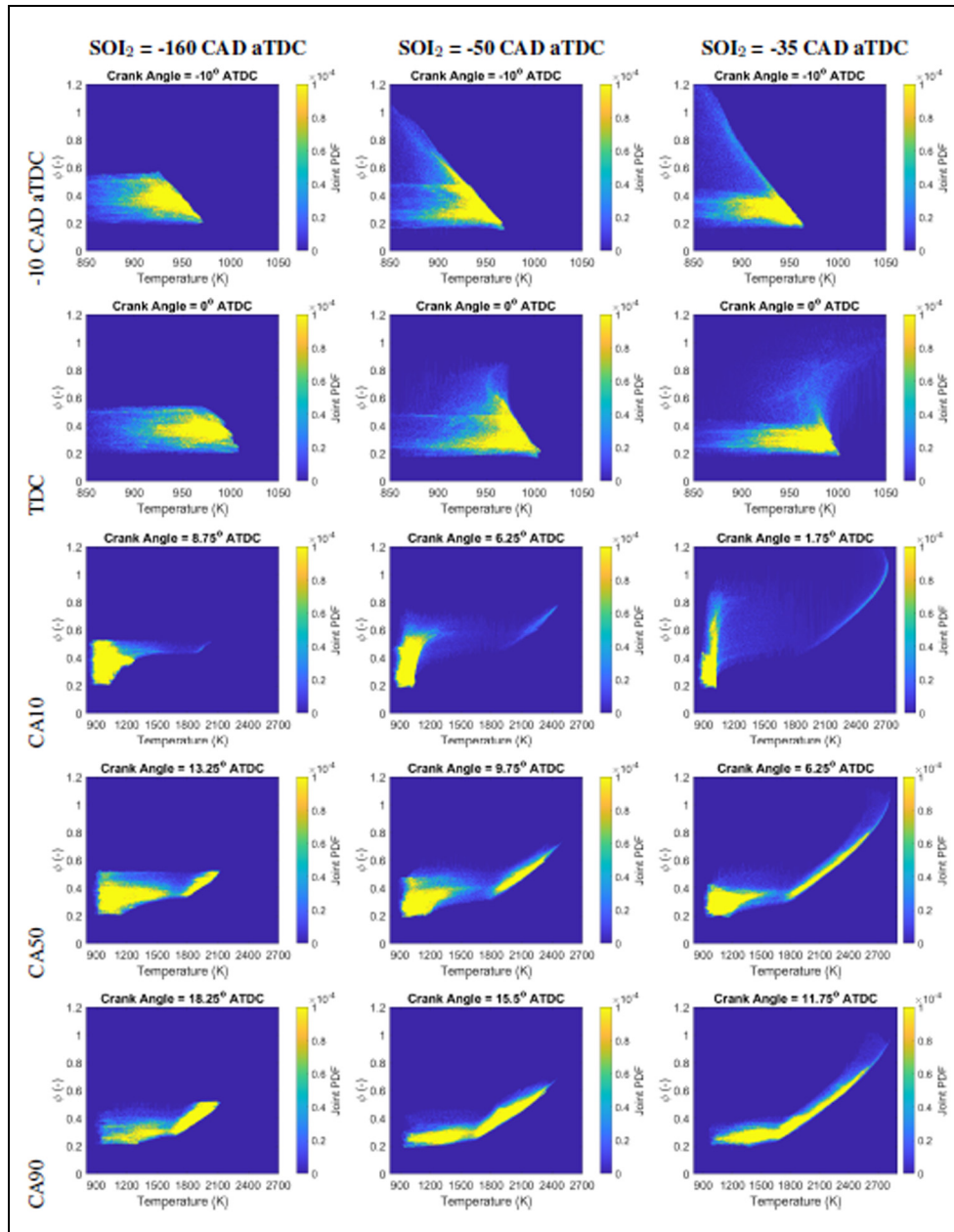
Figure A1. Contours of the joint PDF of mass as a function of equivalence ratio and temperature in the combustion chamber for SKM1 at −10 CAD aTDC, TDC, CA10, CA50 and CA90 for the fifth modeled cycle with SOI$_2$ = −160 CAD aTDC (left), SOI$_2$ = −50 CAD aTDC (center) and SOI$_2$ = −35 CAD aTDC (right).
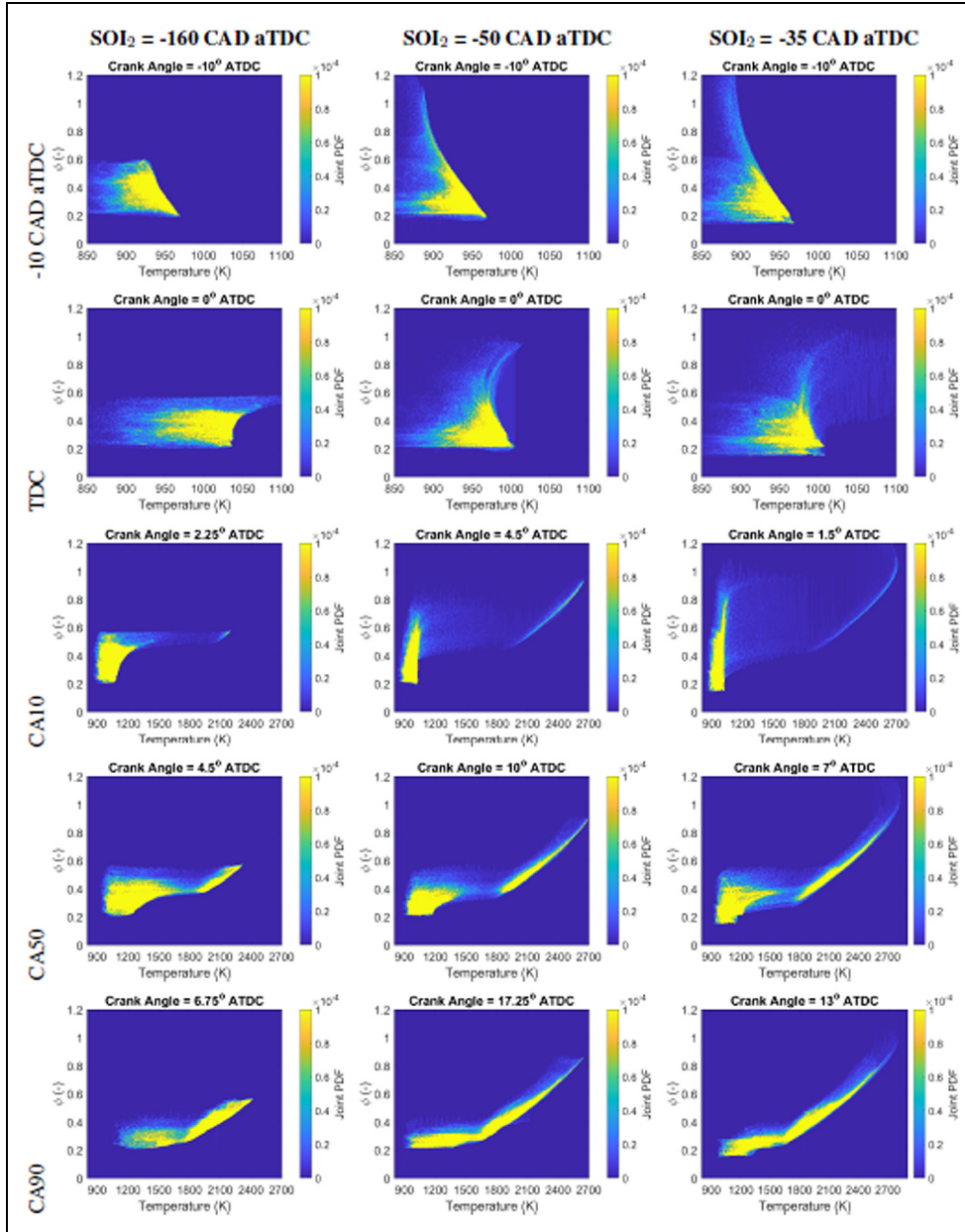
Figure A2. Contours of the joint PDF of mass as a function of equivalence ratio and temperature in the combustion chamber for SKM2 at −10 CAD aTDC, TDC, CA10, CA50 and CA90 for the fifth modeled cycle with SOI₂ = −160 CAD aTDC (left), SOI₂ = −50 CAD aTDC (center), and SOI₂ = −35 CAD aTDC (right).

of −10 CAD aTDC, TDC, CA10, CA50, and CA90 for each operating condition for SKM1 and SKM2 respectively.

Appendix B

Comparison between detailed and reduced mechanisms

Figures B1 and B2 compare the LLNL detailed mechanism against the three reduced mechanisms used in this investigation. Ignition delays were obtained in a 0-D, closed, homogeneous, constant-volume reactor in CHEMKIN-PRO (ignition delay defined as the time of the maximum temperature rise rate). A temperature variation from 700 to 1100 K is plotted at $P = 35$ bar and $\phi = 0.40$ and 1.0 for the species included in the formulation of the surrogates and for the surrogates themselves. In general, the reduced mechanisms replicate reasonably well the results of the detailed mechanism.
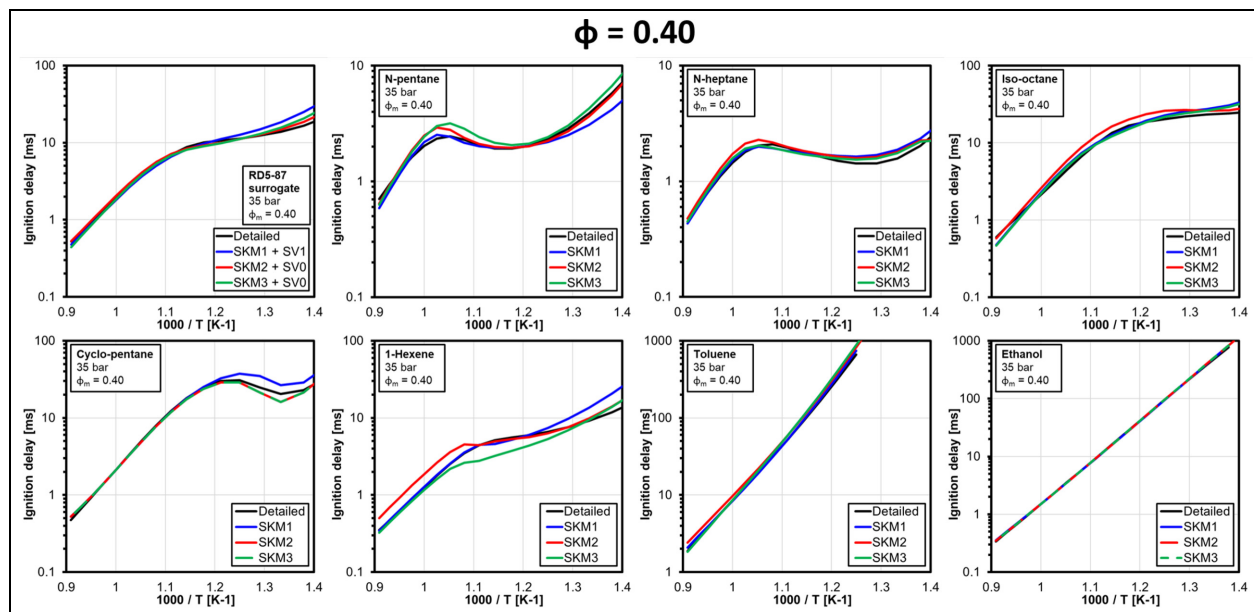
Figure B1. Ignition delay versus temperature for several fuel species at $P = 35$ bar and $\phi = 0.40$ using the detailed mechanism (black), SKM1 (blue), SKM2 (red), and SKM3 (green).
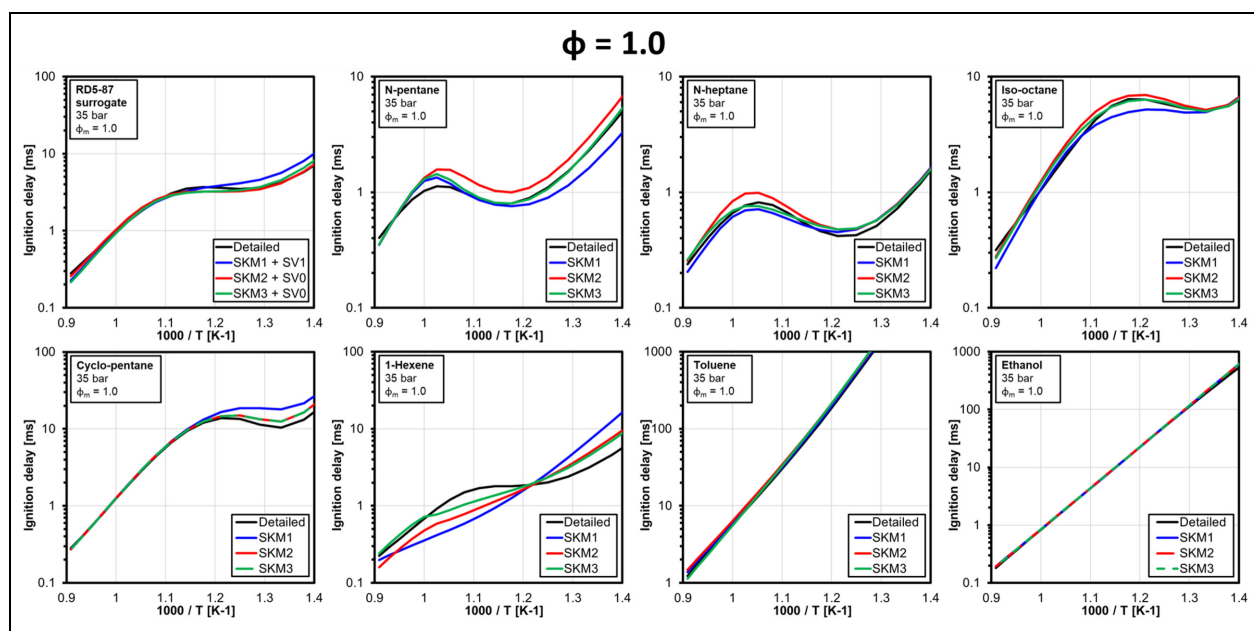
Figure B2. Ignition delay versus temperature for several fuel species at $P = 35$ bar and $\phi = 1.0$ using the detailed mechanism (black), SKM1 (blue), SKM2 (red), and SKM3 (green).